JOURNAL OF GEOPHYSICAL RESEARCH, VOL. 113, A06217, doi:10.1029/2007JA012790, 2008

Nonlinear evolution of the jet-flow-associated Kelvin-Helmholtz instability in MHD plasmas and the formation of Mach-cone-like plane waves

S. H. Lai[1] and L. H. Lyu[1]

Received 4 September 2007; revised 22 March 2008; accepted 7 April 2008; published 18 June 2008.

[1] Kelvin-Helmholtz (K-H) instability triggered by a jet flow along a magnetohydrodynamic (MHD) tangential discontinuity (TD) is studied by means of the two-dimensional MHD simulations. In addition to the vortex structures and the undulant surface waves, we also found fast-mode and slow-mode Mach-cone-like plane waves at the saturation stage of the jet-flow-associated K-H instabilities. Fast-mode Mach-cone-like plane waves are launched in pairs from the ridges of the surface waves when the fast-mode Mach numbers of the surface waves on both sides of the jet flow are greater than one. Slow-mode Mach-cone-like plane waves are found for the first time in a limited range of M_{SL0y}, θ_0, and β_0, where M_{SL0y} is the slow-mode Mach number of the surface disturbances observed in the ambient plasma rest frame, θ_0 is the angle between the surface wave propagation direction and the direction of the ambient magnetic field, and β_0 is the plasma β of the ambient plasma. The flaring angle of the fast-mode Mach-cone-like plane wave is less than or equal to 90°, but the flaring angle of the slow-mode Mach-cone-like plane wave is greater than or equal to 90°. A theoretical model is proposed to explain the formation and the characteristics of the slow-mode Mach-cone-like plane waves. The flaring angles of the slow-mode Mach-cone-like plane waves measured from the simulation results are in good agreement with the flaring angles predicted by the theoretical model. Applications of our results to the observations in the space plasma are discussed.

Citation: Lai, S. H., and L. H. Lyu (2008), Nonlinear evolution of the jet-flow-associated Kelvin-Helmholtz instability in MHD plasmas and the formation of Mach-cone-like plane waves, *J. Geophys. Res.*, *113*, A06217, doi:10.1029/2007JA012790.

1. Introduction

[2] Kelvin-Helmholtz (K-H) instability, also-called velocity shear instability, is triggered by velocity shear. Simulations of the K-H instability in the space plasma have been studied extensively in the past 20 years [e.g., *Miura*, 1982, 1984, 1987, 1990, 1992, 1995, 1997, 1999; *Wu*, 1986; *Manuel and Samson*, 1993; *Thomas and Winske*, 1993; *Otto and Fairfield*, 2000; *Lai and Lyu*, 2006]. Most of the simulation results showed the vortex structures and eddies. *Miura* [1984] found development of slow rarefaction layers near the eddies when the velocity shear is parallel to the ambient magnetic field. In the simulations of the K-H instability at the flank magnetopause, *Miura* [1992] obtained a weak parallel shock in the magnetosheath when the interplanetary magnetic field is sunward or antisunward.

[3] *Lai and Lyu* [2006] obtained the fast-mode nonlinear plane waves at the saturation stage of the K-H instability when the fast-mode Mach number of the surface wave is greater than one. *Lai and Lyu* [2006] proposed a theoretical model based on the formation of the magnetosonic Mach cone to explain the formation of the fast-mode nonlinear plane wave. According to their model, the fast-mode plane waves are generated by the constructive interferences of the fast-mode waves, which are emitted from the ridges of the surface waves and expand based on their group velocities. The flaring angles of the fast-mode plane waves measured from their simulation results are in good agreement with the Mach angles predicted by the theoretical model. Their simulation results and theoretical model of the supermagnetosonic K-H instabilities can explain the sunward steepened wavy structures at the flank magnetopause observed by *Chen and Kivelson* [1993] and *Chen et al.* [1993] under the fast solar wind condition.

[4] Since the theoretical model of the magnetosonic Mach cone proposed by *Lai and Lyu* [2006] can successfully explain the formation of the fast-mode plane waves, we expect that a similar theoretical model should be able to explain the formation of the slow-mode plane wave if we could find one from the simulation of K-H instability. According to the group-velocity Friedrichs diagram, the distribution of the slow-mode group velocity is nearly magnetic field-aligned, which is quite different from the distribution of the fast-mode group velocity. Thus, we expect that the spatial distribution of the slow-mode

[1]Institute of Space Science, National Central University, Chung-Li, Taiwan.

0148-0227/08/2007JA012790$09.00

Mach-cone-like plane wave should be very different from the spatial distribution of the fast-mode Mach-cone-like plane wave. In this study, we will extend the theoretical model proposed by *Lai and Lyu* [2006] to examine the slow-mode Mach-cone-like plane waves found in the simulations of jet-flow-associated K-H instability.

[5] The jet-flow-associated K-H instabilities are expected to take place near the localized high-speed flows, since the localized high-speed flow is accompanied by the strong velocity shear. In Earth's magnetosphere, the localized high-speed plasma flows have been observed at the dayside magnetopause [e.g., *Paschmann et al.*, 1979]. In addition to the dayside magnetopause, the high-speed flows have also been observed in the plasma sheet. After the first systematical study of the high-speed flows in the plasma sheet during plasma sheet expansion by *Lui et al.* [1977], the high-speed plasma flows in the plasma sheet have been studied extensively in the past 20 years [e.g., *Huang and Frank*, 1986; *Baumjohann et al.*, 1990; *Nakamura et al.*, 1991, 2001; *Angelopoulos et al.*, 1992; 1994, 1996, 1999; *Slavin et al.*, 1997; *Cao et al.*, 2006]. The observations showed that most of the high-speed flows in the plasma sheet are bursty, earthward, and spatially localized.

[6] The jet-flow-associated K-H instabilities have been studied from a number of numerical simulations. *Yoon et al.* [1996] have investigated the K-H instability in a dawn-dusk localized plasma flow in the near-Earth current sheet region by means of the Hall- magnetohydrodynamic theory and simulation. They found pairs of compressional perturbations propagating away from the plasma flow along the north and south directions in the magnetotail. A kinetic simulation of the K-H instability in a finite sized jet has been carried out by *Thomas* [1995]. He obtained irregular vortex-type surface waves when the jet is submagnetosonic. The jet-flow-associated K-H instability has also been studied by means of the hydrodynamic simulation [e.g., *Norman et al.*, 1982; *Bodo et al.*, 1994, 1995; *Martí et al.*, 2004] and the magnetohydrodynamic (MHD) simulation [e.g., *Baty and Keppens*, 2002, 2006]. Shock-like structures are found on two sides of the jet flows when the neutral jet flow is supersonic or the MHD jet flow is super-Alfvénic.

[7] In this paper, we study the jet-flow-associated K-H instability at an MHD tangential discontinuity (TD) by means of the two-dimensional MHD simulations. The simulation model and the initial conditions are given in section 2. Both fast-mode nonlinear plane waves and slow-mode nonlinear plane waves are found in the simulations of jet-flow-associated K-H instability, which will be presented in section 3. The theoretical models that explain the formation of these nonlinear plane waves will be given in section 4. We summarize our results in section 5. The applications and the limitations of our results are discussed in section 6.

2. Simulation Model

[8] The jet-flow-associated Kelvin-Helmholtz instability is studied by means of the two-dimensional MHD simulations at a tangential discontinuity (TD). The simulation code is written based on the second-order Lax-Wendroff scheme. The basic equations used in the simulation are the ideal MHD equations, which can be written in the following form.

$$\frac{\partial \rho}{\partial t} + \nabla \cdot (\rho \mathbf{V}) = 0 \tag{1}$$

$$\frac{\partial}{\partial t}(\rho \mathbf{V}) + \nabla \cdot \left(\rho \mathbf{V}\mathbf{V} - \frac{\mathbf{B}\mathbf{B}}{\mu_0}\right) + \nabla\left(p + \frac{B^2}{2\mu_0}\right) = 0 \tag{2}$$

$$\frac{\partial}{\partial t}\left(\frac{1}{2}\rho V^2 + \frac{3p}{2} + \frac{B^2}{2\mu_0}\right) + \nabla \cdot \left[\left(\frac{1}{2}\rho V^2 + \frac{5p}{2} + \frac{B^2}{\mu_0}\right)\mathbf{V} - \frac{\mathbf{B}\,(\mathbf{B}\cdot\mathbf{V})}{\mu_0}\right] = 0 \tag{3}$$

$$\frac{\partial \mathbf{B}}{\partial t} = \nabla \times (\mathbf{V} \times \mathbf{B}) \tag{4}$$

$$\nabla \cdot \mathbf{B} = 0 \tag{5}$$

where $\mathbf{B}$, ρ, $\mathbf{V}$, and p are the magnetic field, the plasma mass density, the plasma bulk velocity, and the plasma thermal pressure, respectively. The MHD Ohm's law $\mathbf{E} + \mathbf{V} \times \mathbf{B} = 0$ has been used to eliminate the electric field in the Faraday's law (equation (4)) and in the energy equation (equation (3)).

[9] In our two-dimensional simulations, all the physical quantities are assumed to be uniform in the z direction, i.e., $\nabla = \hat{\mathbf{x}}(\partial/\partial x) + \hat{\mathbf{y}}(\partial/\partial y)$, where the x direction is the normal direction of the TD, and the y direction is the surface wave propagation direction. The plane of the TD is located at $x = 0$.

[10] For a TD, the normal component of the background magnetic field is equal to zero, i.e., $B_{0x} = 0$. A hyperbolic tangent function is used to set up the transition of the background equilibrium states across the TD. That is,

$$A_0(x) = \frac{A_{02} + A_{01}}{2} + \frac{A_{02} - A_{01}}{2}\tanh\left(\frac{x}{w/3}\right) \tag{6}$$

where $A_0(x)$ denotes the equilibrium state $B_{0y}(x)$, $B_{0z}(x)$, or $\rho_0(x)$, and w is the width of the transition layer of the TD. We choose w to be the normalization length in our simulations. Variables with subscripts "1" and "2" denote the equilibrium states at $x \ll 0$ and $x \gg 0$, respectively. The jet flow is also located at $x = 0$ with a width w_j. The direction of the jet flow is along the y direction. The background equilibrium velocity field $\mathbf{V}_0(x)$ is given by

$$\mathbf{V}_0(x) = V_{0y}(x)\hat{\mathbf{y}} = \frac{V_{J0}}{2}\left[\tanh\left(\frac{x + 0.5w_j}{w/3}\right) - \tanh\left(\frac{x - 0.5w_j}{w/3}\right)\right]\hat{\mathbf{y}} \tag{7}$$

where V_{J0} is the speed of the jet flow at $x = 0$. In order to keep the jet-flow-associated surface disturbances propagating at a relatively constant speed, we choose the width of the jet flow, w_j, to be at least three times wider than the width of the transition layer, w. For convenience, we shall call the uniform medium on the left-hand side and right-

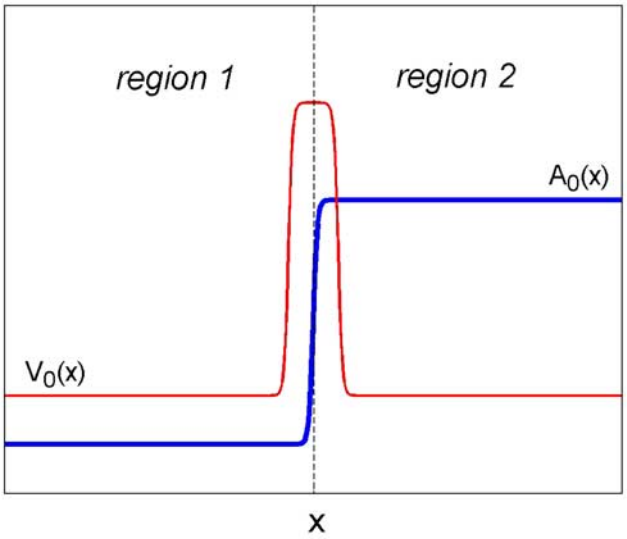

Figure 1. A sketch of the spatial profiles of the background equilibrium states used in this study. The thick curve denotes the profile of $A_0(x)$, which can be $B_{0y}(x)$, $B_{0z}(x)$, or $\rho_0(x)$. The thin curve denotes the profile of $V_{0y}(x)$. The vertical dashed line indicates the location of $x = 0$.

hand side of the jet flow the region 1 and region 2, respectively. Namely, the region 1 is approximately the region with $x < -(w_j + w)/2$ and the region 2 is approximately the region with $x > +(w_j + w)/2$.

[11] Figure 1 is a sketch of the profiles of the background equilibrium states. The thick curve denotes the profile of $A_0(x)$. The thin curve denotes the profile of $V_{0y}(x)$. The vertical dashed line indicates the location of $x = 0$.

[12] Since the total pressure, i.e., the sum of the thermal pressure and the magnetic pressure, is uniform across the TD, we choose the initial background thermal pressure $p_0(x)$ to be

$$p_0(x) = p_{01} + B_{01}^2/2\mu_0 - \left[B_{0y}^2(x) + B_{0z}^2(x)\right]/2\mu_0 \tag{8}$$

The simulation is performed in a simulation box $L_x \times L_y = 100w \times 50w$. The grid size is chosen to be $\Delta_x = \Delta_y = 0.25w$. A uniform boundary condition ($\partial/\partial x = 0$) is imposed at $x = \pm 50w$. A periodic boundary condition is imposed at $y = \pm 25w$. An initial velocity perturbation, $\delta\mathbf{v} = \delta v_x\hat{\mathbf{x}} + \delta v_y\hat{\mathbf{y}}$, which satisfies $\nabla \cdot \delta\mathbf{v} = 0$, is applied to the transition layer of the TD at $t = 0$, where δv_x and δv_y are chosen to be

$$\delta v_x(x,y) = -\delta v_0 \mathrm{sech}\left(\frac{x}{w/3}\right)\sin\left(\frac{2\pi y}{\lambda_y}\right) \tag{9}$$

$$\delta v_y(x,y) = \delta v_0 \frac{3\lambda_y}{2\pi w}\mathrm{sech}\left(\frac{x}{w/3}\right)\tanh\left(\frac{x}{w/3}\right)\cos\left(\frac{2\pi y}{\lambda_y}\right) \tag{10}$$

[13] As we can see, the initial perturbation is periodic along the y direction but localized in the x direction around $x = 0$. The wavelength of the periodic perturbation is λ_y. The peak amplitude of the initial velocity perturbation is δv_0. We choose $\lambda_y = L_y/4 = 12.5w$ and $\delta v_0 = 0.001\ V_{J0}$ in all the simulation cases presented in section 3.

3. Simulation Results

[14] Twenty of our simulation results are listed in Table 1 and Table 2. Table 1 shows the equilibrium states and the simulation results. The normalization constants V_a, B_a, ρ_a, and p_a satisfy the following relations $V_a = B_a/\sqrt{\mu_0\rho_a}$ and $p_a = B_a^2/2\mu_0$. The angles θ_{01} and θ_{02} listed in Table 1 are the angles between the y axis and the background magnetic field $\mathbf{B}_{01}$ and $\mathbf{B}_{02}$, respectively. The values of β_{01} and β_{02} listed in Table 1 are defined by $p_{01}/(B_{01}^2/2\mu_0)$ and $p_{02}/(B_{02}^2/2\mu_0)$, respectively. The phase velocity of the surface waves is $U_{sy}\hat{\mathbf{y}}$, where U_{sy} can be measured from the simulation results. The relative speeds $U_{sy} - V_{0y1}$ and $U_{sy} - V_{0y2}$ listed in Table 2 are the phase speeds of the surface wave observed in the region 1 and region 2 plasma rest frames, respectively.

[15] Before we introduce the Mach numbers to be used in this study, we shall first introduce three MHD wave modes that propagate along the y direction. The phase speeds of the three wave modes are the slow-mode wave speed C_{SL0y}, the intermediate-mode wave speed C_{I0y}, and the fast-mode wave speed C_{F0y}. Their magnitude can be determined by

$$C_{SL0y}^2 = \frac{1}{2}\left\{C_{A0}^2 + C_{S0}^2 - \sqrt{\left(C_{A0}^2 + C_{S0}^2\right)^2 - 4C_{A0}^2C_{S0}^2\cos^2\theta_0}\right\} \tag{11}$$

$$C_{I0y}^2 = (B_0\cos\theta_0)^2/\mu_0\rho_0 \tag{12}$$

$$C_{F0y}^2 = \frac{1}{2}\left\{C_{A0}^2 + C_{S0}^2 + \sqrt{\left(C_{A0}^2 + C_{S0}^2\right)^2 - 4C_{A0}^2C_{S0}^2\cos^2\theta_0}\right\} \tag{13}$$

where $C_{A0}^2 = B_0^2/\mu_0\rho_0$, $C_{S0}^2 = \gamma p_0/\rho_0$, and $\gamma = 5/3$. The C_{S0} and C_{A0} are the sound speed and the Alfvén speed of the equilibrium state, respectively.

[16] The Mach numbers of the surface wave listed in Table 2 are defined by

$$M_{SL0y1}^2 = \left(U_{sy} - V_{0y1}\right)^2/C_{SL0y1}^2 \tag{14}$$

$$M_{SL0y2}^2 = \left(U_{sy} - V_{0y2}\right)^2/C_{SL0y2}^2 \tag{15}$$

$$M_{I0y1}^2 = \left(U_{sy} - V_{0y1}\right)^2/C_{I0y1}^2 \tag{16}$$

$$M_{I0y2}^2 = \left(U_{sy} - V_{0y2}\right)^2/C_{I0y2}^2 \tag{17}$$

$$M_{F0y1}^2 = \left(U_{sy} - V_{0y1}\right)^2/C_{F0y1}^2 \tag{18}$$

Table 1. Background Equilibrium Fields and Simulation Results

Case	Background Equilibrium Fields									Simulation Results		
	$\frac{\rho_{01}}{\rho_a}$	$\frac{\rho_{02}}{\rho_a}$	$\frac{V_{J0}}{V_a}$	$\frac{p_{01}}{p_a}$	$\frac{B_{01}}{B_a}$	$\frac{B_{02}}{B_a}$	θ_{01}	θ_{02}	$\frac{w_j}{w}$	β_{01}	β_{02}	Type
1	1	1	2.5	2	1.50	1.40	9°	9°	4.0	0.89	1.17	**V**
2	1	1	2.5	2	0.80	0.60	0°	0°	4.0	3.13	6.33	**S**
3	1	1	5.0	2	1.50	1.40	0°	0°	4.0	0.89	1.17	**S + FP**
4	1	1	3.3	2	1.50	1.40	0°	0°	4.0	0.89	1.17	**S + SP**
5	1	1	2.5	2	0.80	0.60	0°	180°	4.0	3.13	6.33	**S**
6	1	1	5.0	2	1.50	1.40	90°	90°	4.0	0.89	1.17	**S + FP**
7	1	1	5.0	2	1.50	1.40	0°	180°	4.0	0.89	1.17	**S + FP**
8	1	1	5.0	2	1.50	1.40	20°	20°	4.0	0.89	1.17	**S + FP**
9	1	1	3.4	2	1.50	1.40	20°	20°	4.0	0.89	1.17	**S + SP**
10	1	1	3.0	2	0.80	1.25	0°	180°	0.5	3.13	0.69	**S + SP**
11	1	1	2.5	2	0.91	0.83	0°	0°	4.0	2.40	3.80	**S + SP**
12	1	1	2.3	2	0.91	0.83	20°	20°	4.0	2.40	3.80	**S + SP**
13	1	1	3.1	2	1.50	1.40	0°	0°	4.0	0.89	1.17	**S + SP**
14	1	1	3.5	2	1.50	1.40	0°	0°	4.0	0.89	1.17	**S + SP**
15	1	1	2.2	2	0.91	0.83	0°	0°	4.0	2.40	3.80	**S + SP**
16	1	1	2.4	2	0.91	0.83	0°	0°	4.0	2.40	3.80	**S + SP**
17	1	1	3.2	2	1.50	1.40	20°	20°	4.0	0.89	1.17	**S + SP**
18	1	1	3.0	2	1.50	1.40	20°	20°	4.0	0.89	1.17	**S + SP**
19	1	1	2.0	2	0.91	0.83	20°	20°	4.0	2.40	3.80	**S + SP**
20	1	1	2.35	2	0.91	0.83	20°	20°	4.0	2.40	3.80	**S + SP**

$$M_{F0y2}^2 = \left(U_{sy} - V_{0y2}\right)^2 / C_{F0y2}^2 \tag{19}$$

The Mach numbers $M_{SL0y1,2}$, $M_{I0y1,2}$, and $M_{F0y1,2}$ are the slow-mode Mach numbers, the intermediate-mode Mach numbers, and the fast-mode Mach numbers of the surface wave observed in regions 1 and 2, respectively.

[17] Figure 2 shows the gray-level plots of the normalized plasma density ρ/ρ_a of Case 1 at $t = 87.5\tau_a$ and the movie of the normalized magnetic field strength B/B_a at $t = 0 \sim 200\tau_a$, where $\tau_a = w/V_a$ is the normalization timescale (auxiliary material).[1] Case 1 is characterized by $\theta_{01} = \theta_{02} = 90°$, $M_{F0y1} = 0.4545$, and $M_{F0y2} = 0.4568$. The other parameters of Case 1 are listed in Tables 1 and 2. Since the ambient magnetic fields on both sides of the TD are perpendicular to the simulation plane, there is no magnetic tension force in this two-dimensional simulation. The initial perturbations are amplified by the K-H instability. It can be seen from the movie that the perturbations grow into pairs of vortex structures with opposite vorticities at the saturation stage. The vortex structure is denoted by '**V**' in Table 1. The vortex structures will not merge into a single big vortex, as has been shown in previous studies [e.g., *Miura*, 1999]. This is because voticities of the vortex pairs obtained by *Miura* [1999] are in the same direction, but the vorticities of the vortex pairs found in the present simulation results are in the opposite directions.

[18] Figure 3 shows the gray-level plots of the normalized plasma density ρ/ρ_a and the normalized magnetic field strength B/B_a of Case 2 at $t = 50\tau_a$. Case 2 is characterized by $\theta_{01} = \theta_{02} = 0°$, $M_{F0y1} = 0.8908$, $M_{F0y2} = 0.8343$, $M_{I0y1} = 1.4375$, and $M_{I0y2} = 1.9167$. The ambient magnetic fields on both sides of the TD are parallel to the shear flow. Since the magnetic tension force prevents the initial perturbations from growing into the vortex structures, the perturbations grow into S-shaped undulant surface waves at the saturation stage. The propagation direction of the S-shaped surface waves is along the $+y$ direction with respect to the plasmas in region 1 and region 2, but along the $-y$ direction with respect to the jet flow. The S-shaped surface wave is denoted by "**S**" in Table 1. The S-shaped surface waves can also be found when $\theta_{01} = 0°$ and $\theta_{02} = 180°$ (e.g., Case 5).

[19] Figure 4 shows the gray-level plots of the normalized plasma density ρ/ρ_a and the normalized magnetic field strength B/B_a of Case 3 at $t = 30\tau_a$. Case 3 is characterized by $\theta_{01} = \theta_{02} = 0°$, $M_{F0y1} = 1.6667$ and $M_{F0y2} = 1.7857$. The velocity shear of the jet flow is much higher than the fast-mode speed of the background plasma. The initial perturbations are unstable to the K-H instability. They grow into the S-shaped surface waves, which propagate along the $+y$ direction in the region 1 and region 2 plasma rest frames but along the $-y$ direction in the jet flow rest frame. Since we choose the wavelength of the initial perturbations to be one fourth of the system length along the y direction ($\lambda_y = L_y/4$), four pairs of the nonlinear plane waves are developed from the ridges of the S-shaped surface waves. The phase relations between the density perturbation $\delta\rho$ and the magnetic field strength perturbation δB can help us to determine the wave mode of the plane waves.

[20] Figure 5 shows the cross section of the plasma density and the magnetic field strength of Case 3 at three fixed locations $x = -6.0w$ (region 1) (Figure 5a), $x = 0$ (Figure 5b), and $x = 6.0w$ (region 2) (Figure 5c) along the y direction at $t = 30\tau_a$. The thin curves are the spatial profiles of ρ/ρ_a. The thick curves are the spatial profiles of B/B_a. The two arrows in Figures 5a and 5c indicate the directions of the background plasma flows observed in the surface-wave rest frame. We can see steepening of the nonlinear waves on the upstream side in both Figure 5a and Figure 5c. The perturbations of the plasma density and the magnetic field strength are in-phase in both region 1 and region 2. Thus, the plane waves are the fast-mode plane waves. This type of simulation results, which consist of the S-shaped surface waves and the fast-mode nonlinear plane waves, is denoted by "**S + FP**" in Table 1. The fast-mode nonlinear plane waves can also be found at other θ_0 and β_0 as long as the fast-mode Mach number of the surface wave (M_{F0y}) is greater than one (e.g., Cases 6–8 as listed in Tables 1 and 2).

[21] Figure 6 shows the gray-level plots of the normalized plasma density ρ/ρ_a and the normalized magnetic field strength B/B_a of Case 4 at $t = 100\tau_a$. Case 4 is characterized by $\theta_{01} = \theta_{02} = 0°$, $M_{SL0y1} = 0.8521$, and $M_{SL0y2} = 0.7963$. Note that both M_{SL0y1} and M_{SL0y2} are less than one. The initial perturbations grow into the S-shaped surface waves, which propagate along the $+y$ direction with respect to the plasmas in region 1 and region 2 but along the $-y$ direction with respect to the jet flow. Four pairs of nonlinear plane waves are developed from the ridges of the S-shaped surface waves.

[22] Figure 7 shows the cross section of the plasma density and the magnetic field strength of Case 4 at three different locations $x = -6.0w$ (region 1) (Figure 7a), $x = 0$ (Figure 7b), and $x = 6.0w$ (region 2) (Figure 7c) along the y direction at $t = 100\tau_a$. The thin curves are the spatial profiles of ρ/ρ_a and the thick curves are the spatial profiles of $(B/B_a) - c_0$, where the offset constant c_0 is chosen such

[1] Auxiliary materials are available in the HTML. doi:10.1029/2007JA012790.

Table 2. Mach Numbers Obtained From Simulation Results

Case	$\frac{U_{sy}}{V_a}$	$\frac{U_{sy}-V_{0y1}}{V_a}$	$\frac{U_{sy}-V_{0y2}}{V_a}$	M_{SL0y1}	M_{SL0y2}	M_{I0y1}	M_{I0y2}	M_{F0y1}	M_{F0y2}
1	0.90	0.90	0.90	∞	∞	∞	∞	0.4545	0.4568
2	1.15	1.15	1.15	1.4375	1.9167	1.4375	1.9167	0.8908	0.8343
3	2.50	2.50	2.50	1.9365	1.8098	1.6667	1.7857	1.6667	1.7857
4	1.10	1.10	1.10	0.8521	0.7963	0.7333	0.7857	0.7333	0.7857
5	1.15	1.15	1.15	1.4375	1.9167	1.4375	1.9167	0.8908	0.8343
6	2.60	2.60	2.60	∞	∞	∞	∞	1.3138	1.3219
7	2.50	2.50	2.50	1.9365	1.8098	1.6667	1.7857	1.6667	1.7857
8	2.60	2.60	2.60	2.3400	2.3052	1.8446	1.9763	1.5876	1.6136
9	1.10	1.10	1.10	0.9900	0.9753	0.7804	0.8361	0.6717	0.6827
10	0.90	0.90	0.90	1.1250	0.9498	1.1250	0.7200	0.6971	0.7200
11	0.77	0.77	0.77	0.8434	0.9244	0.8434	0.9244	0.5964	0.5766
12	0.75	0.75	0.75	0.9160	0.9898	0.8742	0.9581	0.6717	0.6827
13	0.95	0.95	0.95	0.7746	0.7239	0.6333	0.6786	0.6333	0.6786
14	1.23	1.23	1.23	0.9527	0.8904	0.8200	0.8786	0.8200	0.8786
15	0.83	0.83	0.83	0.9090	0.9964	0.9090	0.9964	0.6429	0.6216
16	0.75	0.75	0.75	0.8215	0.9003	0.8215	0.9003	0.5809	0.5617
17	1.00	1.00	1.00	0.9000	0.8866	0.7095	0.7601	0.6106	0.6206
18	0.95	0.95	0.95	0.8551	0.8423	0.6740	0.7221	0.5801	0.5890
19	0.74	0.74	0.74	0.9037	0.9766	0.8625	0.9453	0.5471	0.5365
20	0.71	0.71	0.71	0.8610	0.9304	0.8217	0.9006	0.5218	0.5111

that the thin curve and the thick curve can be plotted in the same scale. The two arrows in Figures 7a and 7c indicate the directions of the background plasma flows observed in the surface-wave rest frame. We can see steepening of the density profiles on the upstream side in both Figure 7a and Figure 7c. The perturbations of the plasma density and the magnetic field strength are out-of-phase in both region 1 and region 2. Thus, the plane waves are the slow-mode plane waves. This type of simulation results, which consist of the S-shaped surface waves and the slow-mode nonlinear plane waves, is denoted by "**S + SP**" in Table 1. The slow-mode nonlinear plane waves can also be found in Cases 9–20 as listed in Tables 1 and 2.

[23] Unlike the fast-mode nonlinear plane wave, the slow-mode nonlinear plane wave can only be found in a limited range of M_{SL0y}, β_0, and θ_0. The two-dimensional distribution of the slow-mode plane waves shown in Figure 6 is also different from the spatial distribution of the fast-mode plane

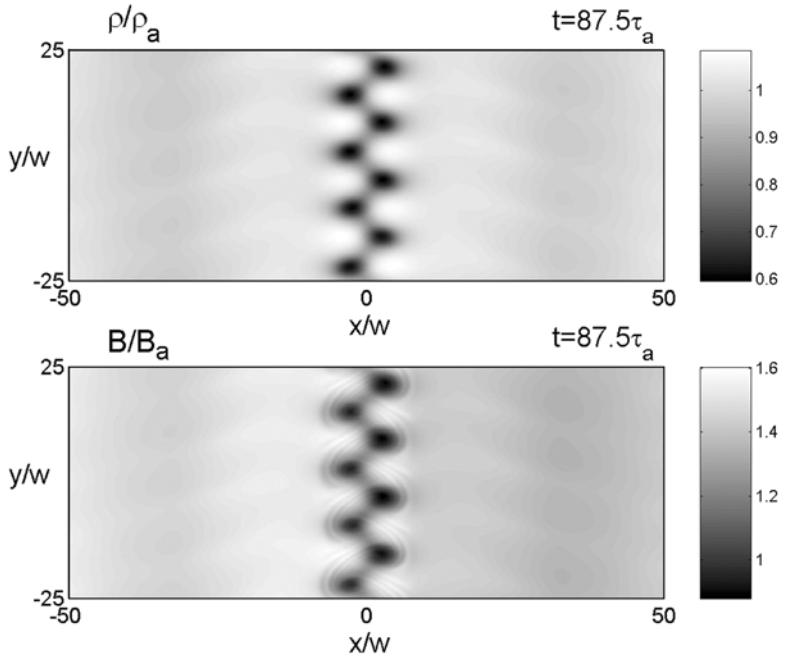

Figure 2. Gray-level plots of (top) the plasma density ρ/ρ_a of Case 1 at $t = 87.5\tau_a$ and (bottom) the still of Animation S1 in the auxiliary material of the normalized magnetic field strength B/B_a at $t = 0 \sim 200\tau_a$. Case 1 is characterized by $\theta_{01} = \theta_{02} = 90°$, $M_{F0y1} = 0.4545$, and $M_{F0y2} = 0.4568$. The initial perturbations are unstable to the K-H instability. It can be seen from Animation S1 in the auxiliary material that the perturbations grow into pairs of vortex structures with opposite vorticities at the saturation stage. The vortex structure is denoted by "**V**" in Table 1.

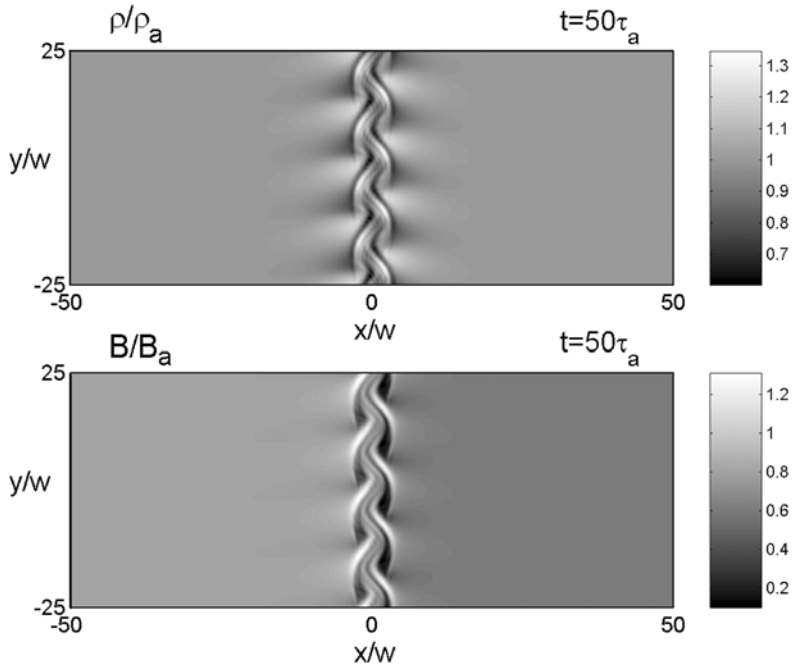

Figure 3. Gray-level plots of ρ/ρ_a and B/B_a obtained at the nonlinear stage of Case 2 at $t = 50\tau_a$. Case 2 is characterized by $\theta_{01} = \theta_{02} = 0°$, $M_{F0y1} < 1$, $M_{F0y2} < 1$, $M_{I0y1} > 1$, and $M_{I0y2} > 1$. The initial perturbations are unstable to the K-H instability. They grow into S-shaped undulate surface waves at the saturation stage. The propagation direction of the S-shaped surface waves is along the $+y$ direction with respect to the plasmas in region 1 and region 2 but along the $-y$ direction with respect to the jet flow. The S-shaped surface wave is denoted by "**S**" in Table 1.

waves shown in Figure 4. In the next section, we will discuss the mechanisms that could lead to the formation of the fast-mode plane waves and the slow-mode plane waves found in our simulations.

4. Formation of the Nonlinear Plane Waves

[24] The theoretical model of the magnetosonic Mach cone proposed by *Lai and Lyu* [2006] has successfully explained the formation of the fast-mode plane waves. We expect that a similar theoretical model should be able to explain the formation of the slow-mode plane wave found in this study.

[25] We will briefly review the fast-mode nonlinear plane wave in section 4.1. We will then propose a theoretical model, similar to the one proposed by *Lai and Lyu* [2006], to explain the formation of the slow-mode nonlinear plane wave in section 4.2.

4.1. Formation of the Fast-Mode Nonlinear Plane Waves

[26] The simulation results of *Lai and Lyu* [2006] found that the fast-mode plane waves are launched from the ridges of the surface waves when $M_{F0y} \geq 1$. The strong Mach number dependence has provided useful information that helps them to identify the cause of the nonlinear fast-mode plane waves in their simulation. They proposed that the formation of these nonlinear waves should be similar to the formation of the sonic Mach cone in the gasdynamics. In their study, they use free-hand sketches to illustrate the formation of the sonic/magnetosonic Mach cone.

[27] After some lengthy derivations, they showed that the flaring angle α of the fast-mode solitary wave is a function of the fast-mode Mach number M_{F0y}, the plasma beta β_0, and the angle θ_0, which is the acute angle between the ambient magnetic field and the y axis. The flaring angle of the fast-mode solitary wave is given by

$$\alpha = \sin^{-1}\sqrt{\frac{(\gamma\beta_0/2)+1}{M_{F0y}^2\left(C_{F0y}^2/C_{A0}^2\right)} - \frac{(\gamma\beta_0/2)\cos^2\theta_0}{M_{F0y}^4\left(C_{F0y}^2/C_{A0}^2\right)^2}}$$

[28] In this section, we use a simulation event as an example to demonstrate the constructive interference process intuitively. We calculate the wavefronts of the waves emitted from a moving point source by assuming that the wavefronts expand based on the fast-mode group velocity. We then show the flaring angle of the constructive interference layer is the same as the flaring angle of the nonlinear waves obtained in the simulation.

[29] Figure 8 shows an example of the formation of the fast-mode Mach-cone-like nonlinear waves. We choose the region 2 equilibrium state of Case 3 as an example to compute the propagation and the constructive interference of the fast-mode waves emitted from a moving point source numerically. Points $S_0 \sim S_6$ denote the locations of the point source at $t = t_0 \sim t_0 + 6\Delta t$, respectively. The propagation speed of the point source relative to the background medium is $(U_{sy} - V_{0y})$, which is equal to the phase speed of the surface wave observed in the region 2 plasma rest frame of Case 3. The propagation speed of the point source

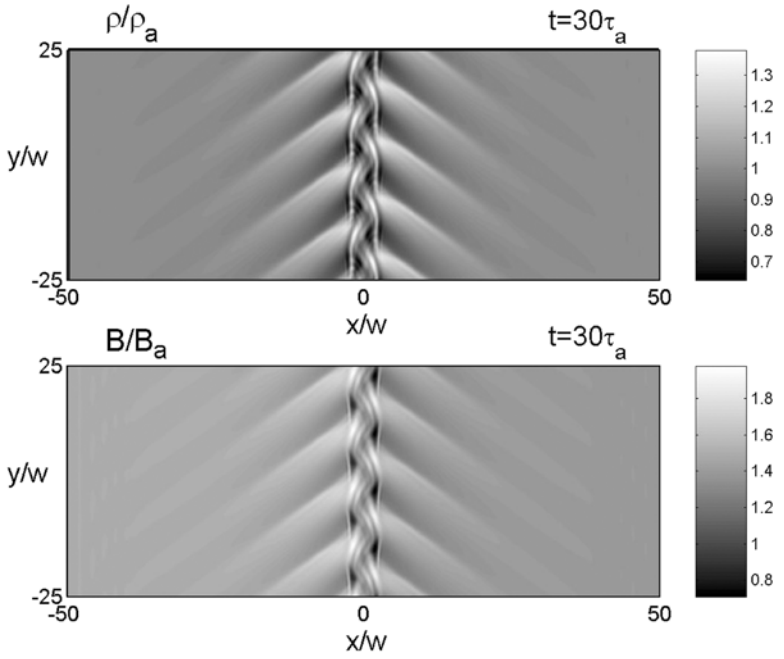

Figure 4. Gray-level plots of ρ/ρ_a and B/B_a obtained at the nonlinear stage of Case 3 at $t = 30\tau_a$. Case 3 is characterized by $\theta_{01} = \theta_{02} = 0°$, $M_{F0y1} > 1$, and $M_{F0y2} > 1$. The initial perturbations are unstable to the K-H instability. They grow into the S-shaped surface waves. These S-shaped surface waves propagate along the $+y$ direction in the region 1 and region 2 plasma rest frames but along the $-y$ direction in the jet-flow plasma rest frame. Four pairs of nonlinear plane waves are developed from the ridges of the S-shaped surface waves. It will be shown in Figure 5 that these nonlinear waves are fast-mode waves. This type of simulation results, which consist of the S-shaped surface waves and the fast-mode nonlinear plane waves, is denoted by "**S + FP**" in Table 1.

is greater than the fast-mode speed in the y direction. We compute the location of the wavefront of the fast-mode wave emitted from the moving point source by assuming that the wavefront expands based on fast-mode group velocity. The five dashed ellipses are the computed wavefront locations of the fast-mode wave emitted from point S_0 at the consecutive time interval $t = t_0 + \Delta t \sim t_0 + 5\Delta t$. The point source continuously emits fast-mode waves as it travels from point S_0 to point S_6. At $t = t_0 + 6\Delta t$, the point source reaches to the point S_6. At the same time, the fast-mode waves emitted from the point source, at $t = t_0 \sim t_0 + 5\Delta t$, will expand to different sizes as shown by the solid ellipses. The constructive interferences of these fast-mode waves can result in a pair of magnetosonic Mach-cone-like plane waves as denoted by the thick lines. As we can see, the fast-mode Mach-cone-like plane wave is tangent to the largest solid ellipse at point g. The flaring angle α is defined by the angle between the line S_0S_6 and the thick line S_6g. The flaring angle α is also-called the Mach angle of the magnetosonic Mach-cone-like plane wave. The thin arrow ($\hat{\mathbf{V}}_p$) indicates the direction of the phase velocity of the magnetosonic Mach-cone-like plane wave. The dashed arrow ($\hat{\mathbf{V}}_g$) indicates the direction of the corresponding group velocity of the fast-mode wave. For comparison, we put the gray-level plot of the plasma density of Case 3 on the right-hand side of this wave interference plot. As we can see, the flaring angle of the fast-mode Mach-cone-like plane wave obtained from the simulation is in good agreement with the flaring angle α obtained from this constructive interference calculation.

4.2. Formation of the Slow-Mode Nonlinear Plane Waves

[30] It has been discussed in our previous paper [*Lai and Lyu*, 2006] that the phase velocity and the group velocity of the ordinary sound waves are isotropic and identical to each other in a uniform natural gas medium, therefore there is no difference to use either the phase velocity or the group velocity in determining the Mach cone angle in natural gasdynamics [e.g., *Landau and Lifshitz*, 1987, chap. 9]. In the MHD plasma, the group velocity and the phase velocity are in general not isotropic and not identical to each other. Because the local phase velocity is perpendicular to the line tangent to the point on the wavefront, but the local group velocity is along the line connected to the point source and the point on the wavefront [e.g., *Landau and Lifshitz*, 1987, chap. 8], the propagation direction of the wavefront emitted from a point source should not be parallel to the phase velocity unless the shape of the wavefront is a circle, i.e., unless the wave propagation is isotropic. Thus, we should use the group velocity, not the phase velocity, to determine the Mach cone angle of the MHD waves.

[31] In subsection 4.1, we have shown that the fast-mode wave emitted from a point disturbance will expand based on the group velocity of the fast-mode wave, which is consistent with the discussion given in chapter 8 of *Landau and Lifshitz* [1987]. Thus, we expect that the slow-mode waves

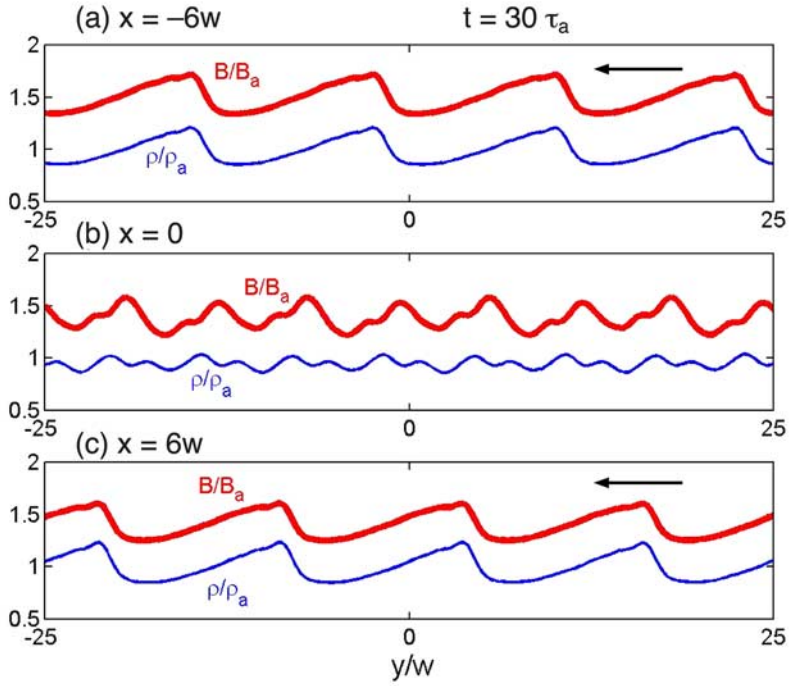

Figure 5. Spatial profiles of the plasma density (the thin curves) and the magnetic field strength (the thick curves) of Case 3 along the y direction at three different locations (a) $x = -6.0w$ (region 1), (b) $x = 0$, and (c) $x = 6.0w$ (region 2) at $t = 30\tau_a$. The variations of the plasma density and the magnetic strength are in-phase in both region 1 and region 2. Thus, the nonlinear plane waves are fast-mode waves. The two arrows shown in Figures 5a and 5c indicate the directions of the background plasma flows observed in the surface-wave rest frame. We can see steepening of the nonlinear waves on the upstream sides in both Figures 5a and 5c.

emitted from a point disturbance should also expand based on the group velocity of the slow-mode wave. We will first review the group velocity distribution of the slow-mode waves. We will then use the equilibrium state of region 2 of Case 4 as an example to compute the wave emitted from a moving point source based on the slow-mode group velocity. A derivation of the analytical form of the flaring angle of the slow-mode Mach-cone-like plane wave will be carried out afterward.

[32] Figure 9 shows the Friedrichs diagrams of the slow-mode group velocity, where $(V_g)_{//\mathbf{B}_0} = \mathbf{V}_g \cdot (\mathbf{B}_0/B_0)$, and $(V_g)_{\perp}\mathbf{B}_0{}^2 = V_g^2 - (V_g)_{//\mathbf{B}_0}{}^2$. Figure 9 shows slow-mode group velocities obtained under the conditions $C_{S0}^2/C_{A0}^2 = 0.5$ ($\beta_0 = 0.6$) (Figure 9a), $C_{S0}^2/C_{A0}^2 = 1.0$ ($\beta_0 = 1.2$) (Figure 9b), and $C_{S0}^2/C_{A0}^2 = 2.0$ ($\beta_0 = 2.4$) (Figure 9c), where $\beta_0 = p_0/(B_0^2/2\mu_0)$. It can be shown that $C_{S0}^2/C_{A0}^2 = \gamma\beta_0/2$. According to Figure 9, the group velocity of the slow-mode waves has the largest perpendicular component to the background magnetic field when $\beta_0 = 1.2$ or $C_{S0}^2 = C_{A0}^2$. As a result, the slow-mode plane waves at $\beta_0 \approx 1.2$ will expand far away from the point source much faster than the slow-mode waves in the cases with $\beta_0 \gg 1.2$ and $\beta_0 \ll 1.2$. Thus, qualitatively, we can expect that the constructive interference of slow-mode waves can easily take place in the simulation when $\beta_0 \approx 1.2$.

[33] Figure 10 shows an example of the formation of the slow-mode Mach-cone-like nonlinear waves. We choose the region 2 equilibrium state of Case 4 as an example to compute the propagation and the constructive interference of the slow-mode waves emitted from a moving point source numerically. Points S_0–S_6 denote the locations of the point source at $t = t_0 \sim t_0 + 6\Delta t$, respectively. The propagation speed of the point source with respect to the background medium is $(U_{sy} - V_{0y})$, which is equal to the phase speed of the surface wave observed in the region 2 plasma rest frame of Case 4. The propagation speed of the point source is less than the slow-mode speed in the y direction. We compute the location of the wavefront of the slow-mode wave emitted from the moving point source by assuming that the wavefront expands based on slow-mode group velocity. The five dashed triangle-like curves are the computed wavefront locations of the slow-mode wave emitted from point S_0 at the consecutive time interval $t = t_0 + \Delta t \sim t_0 + 5\Delta t$. The point source continuously emits slow-mode waves as it travels from point S_0 to point S_6. At $t = t_0 + 6\Delta t$, the point source reaches to the point S_6. At the same time, the slow-mode waves emitted from the point source, at $t = t_0 \sim t_0 + 5\Delta t$, will expand to different locations as shown by the solid triangle-like curves. The constructive interferences of these slow-mode waves can result in a pair of slow-mode Mach-cone-like plane waves as denoted by the thick lines. As we can see, the slow-mode Mach-cone-like plane wave is tangent to the largest solid triangle-like curve at point g. The flaring angle α is defined by the angle between the line S_0S_6 and the thick line S_6g. The flaring angle is greater than

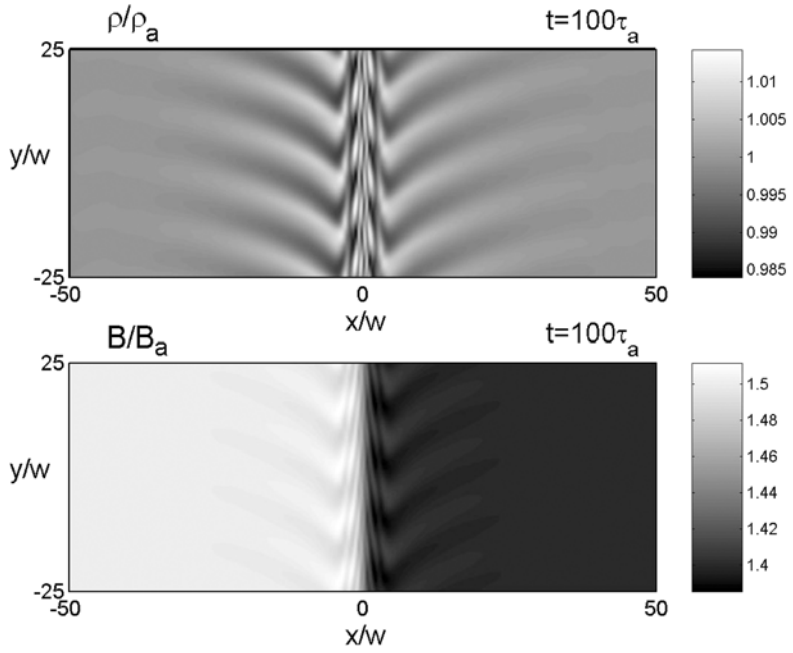

Figure 6. Gray-level plots of ρ/ρ_a and B/B_a obtained at the nonlinear stage of Case 4 at $t = 100\tau_a$. Case 4 is characterized by $\theta_{01} = \theta_{02} = 0°$, $M_{SL0y1} = 0.8521$, and $M_{SL0y2} = 0.7963$. The initial perturbations are unstable to the K-H instability. They grow into the S-shaped surface waves. The S-shaped surface waves propagate along the $+y$ direction in the region 1 and region 2 plasma rest frames but along the $-y$ direction in the jet-flow plasma rest frame. Four pairs of nonlinear plane waves are developed from the ridges of the S-shaped surface waves. It will be shown in Figure 7 that these nonlinear waves are slow-mode waves. This type of simulation results, which consist of the S-shaped surface waves and the slow-mode nonlinear plane waves, is denoted by "**S + SP**" in Table 1.

90°. The thin arrow ($\hat{\mathbf{V}}_p$) indicates the direction of the phase velocity of the slow-mode Mach-cone-like plane wave. The dashed arrow ($\hat{\mathbf{V}}_g$) indicates the direction of the corresponding group velocity of the slow-mode wave. For comparison, we put the gray-level plot of the plasma density of Case 4 on the left-hand side of this wave-interference plot. As we can see, the flaring angle of the slow-mode Mach-cone-like plane wave obtained from the simulation is in good agreement with the flaring angle α obtained from this constructive interference calculation. Note that the slow-mode waves that propagate nearly parallel to the $-y$ direction will not result in constructive interferences. Thus, only the slow-mode waves that propagate nearly parallel to the $+y$ direction are shown in Figure 10.

[34] It can be seen from our simulation results that the extensions of the nonlinear waves extended continuously away from the tips of the nonlinear plane waves and form a curved wavefront, which is associated with the arc *gh* shown in Figure 10. Similar structures are commonly found in the fast-mode Mach-cone-like nonlinear plane waves, which have been discussed in Figure 14 of *Lai and Lyu* [2006]. Note that the absence of curved extension occurs when the constructive interference takes place along the top curve $h'h$ (i.e., if the point *g* is located between points h' and *h*). The Mach angles found in these cases are nearly 90° (not shown).

[35] From Figure 10, we can conclude that the constructive interferences of the slow-mode waves cannot be found when the speed of the point source is greater than the slow-mode speed or less than the minimum of the slow-mode group velocity.

[36] In the two-dimensional simulation, the ridge of the surface wave is a line-type disturbance, which is along the *z* direction. On the basis of a sketch of three-dimension distribution of the surface wave and the fast-mode Mach-cone-like plane wave, *Lai and Lyu* [2006] obtained the theoretical solution of the Mach angle as a function of β_0, θ_0, and M_{F0y}. The flaring angles of the fast-mode Mach-cone-like plane waves measured form their simulation results are in good agreements with the Mach angles predicted by the theoretical model. Similarly, we will derive the theoretical flaring angles of the slow-mode Mach-cone-like plane waves below.

[37] Figure 11 shows how to determine the flaring angle α of the slow-mode Mach-cone-like plane wave for any given M_{SL0y}, β_0, and θ_0. In our two-dimensional simulation, the slow-mode Mach-cone-like plane wave is generated by a line-type disturbance, extended along the *z* direction. Figure 11a shows a line-type disturbance that moves from *ss** to *bb** toward the $-y$ direction with respect to the uniform plasma in region 1 and produces a slow-mode half plane nonlinear wave in region 1. Figure 11b shows a line-type disturbance that moves from *ss** to *bb** toward the $+y$ direction with respect to the uniform plasma in region 2 and produces a slow-mode half plane nonlinear wave in region 2. We assume that the undulant surface wave is confined inside the pink layer. The line-type disturbance moves at a speed $U_{sy} - V_{0y} = M_{SL0y}C_{SL0y}$ relative to the uniform

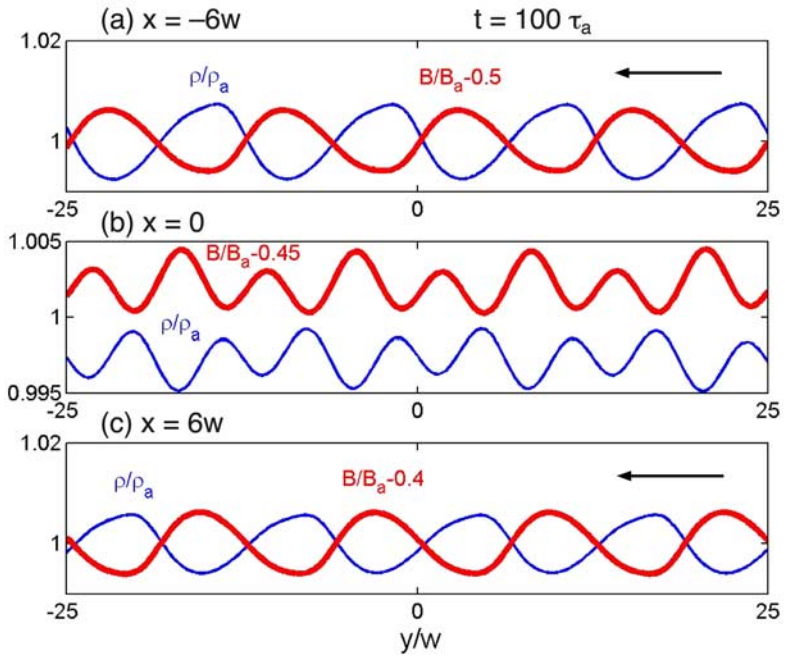

Figure 7. Spatial profiles of the plasma density and the magnetic field strength of Case 4 along the y direction at three different locations (a) $x = -6.0w$ (region 1), (b) $x = 0$, and (c) $x = 6.0w$ (region 2) at $t = 100\tau_a$. The thin curves are the spatial profiles of ρ/ρ_a and the thick curves are the spatial profiles of $(B/B_a) - c_0$, where the offset constant c_0 is chosen such that the thin curve and the thick curve can be plotted in the same scale. The variations of the plasma density and the magnetic strength are out-of-phase in both region 1 and region 2. Thus, the nonlinear plane waves are slow-mode waves. The two arrows shown in Figures 7a and 7c indicate the directions of the background plasma flows observed in the surface-wave rest frame. We can see steepening of the density profiles on the upstream side in both Figures 7a and 7c.

plasma outside the pink layer. The blue plane contains the slow-mode half plane wave. The blue plane and the outer boundary of the pink layer intersect at bb^*. Point a is the intersection of the line bb^* and the magnetic field line that passing through point s. Following the same arguments as discussed in Figure 8 and Figure 10 of *Lai and Lyu* [2006], we have $sb = (U_{sy} - V_{0y})\Delta t = M_{SL0y} C_{SL0y} \Delta t$, $sg = C_{SL0\psi_g}\Delta t$, $C_{SL0\psi_g}\Delta t$, $C_{SL0\psi_g}\Delta t$, and $sc = C_{SL0\psi}\Delta t$ where $C_{SL0\psi}$ is the phase speed

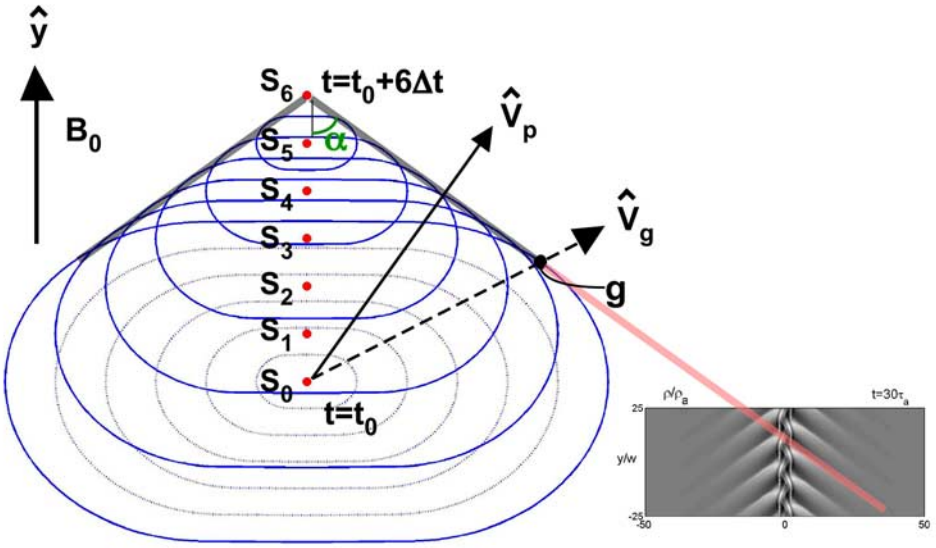

Figure 8. An example to show the formation of the fast-mode Mach-cone-like nonlinear waves. In this example, we choose the region 2 equilibrium state of Case 3 to compute the wavefront locations of the fast-mode waves emitted from a moving point source. See the text for the discussion in detail.

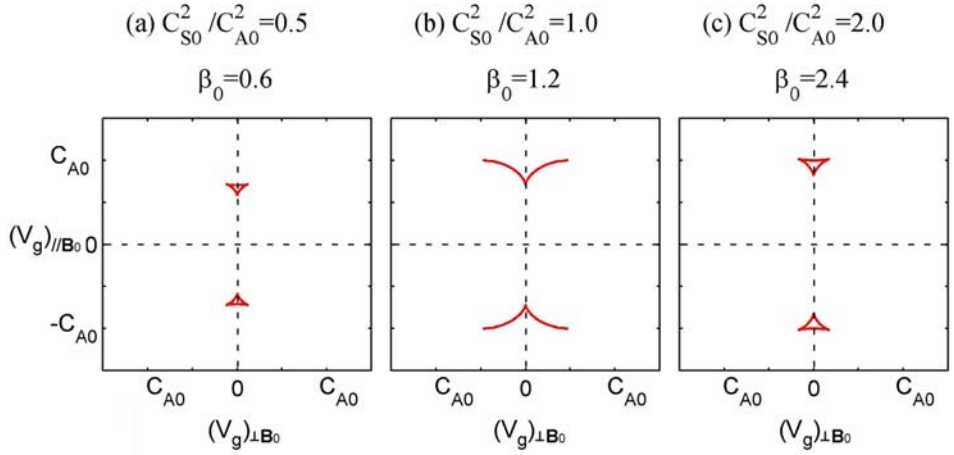

Figure 9. The Friedrichs diagrams of the slow-mode group velocity obtained at (a) $C_{S0}^2/C_{A0}^2 = 0.5$ ($\beta_0 = 0.6$), (b) $C_{S0}^2/C_{A0}^2 = 1.0$ ($\beta_0 = 1.2$), and (c) $C_{S0}^2/C_{A0}^2 = 2.0$ ($\beta_0 = 2.4$), where $(V_g)_{//\mathbf{B}_0} = \mathbf{V}_g \cdot (\mathbf{B}_0/B_0)$, $(V_g)_\perp \mathbf{B}_0^2 = V_g^2 - (V_g)_{//\mathbf{B}_0}^2$, $\beta_0 = p_0/(B_0^2/2\mu_0)$, $C_{A0}^2 = B_0^2/\mu_0\rho_0$, $C_{S0}^2 = \gamma p_0/\rho_0$, and $\gamma = 5/3$. The C_{S0} and C_{A0} are the sound speed and the Alfvén speed of the equilibrium state, respectively. It can be shown that $C_{S0}^2/C_{A0}^2 = \gamma\beta_0/2$. When $\beta_0 = 1.2$, the slow-mode group velocity has the largest perpendicular component to the background magnetic field.

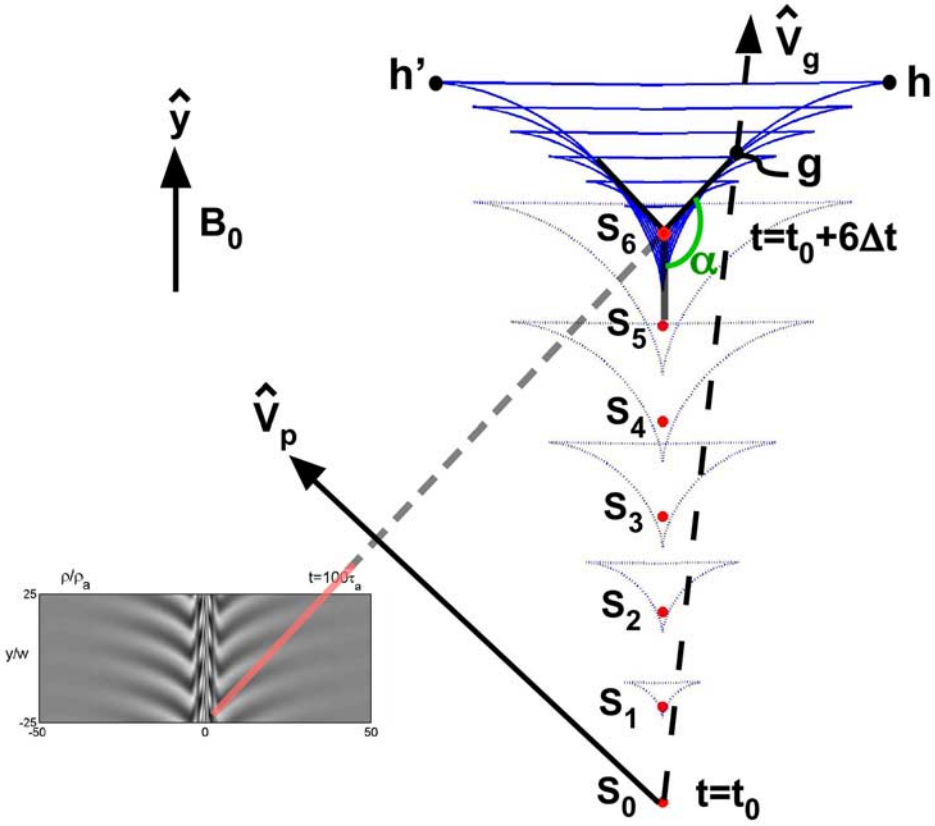

Figure 10. An example to show the formation of the slow-mode Mach-cone-like nonlinear waves. In this example, we choose the region 2 equilibrium state of Case 4 to compute the wavefront locations of the slow-mode waves emitted from a moving point source. See the text for the discussion in detail.

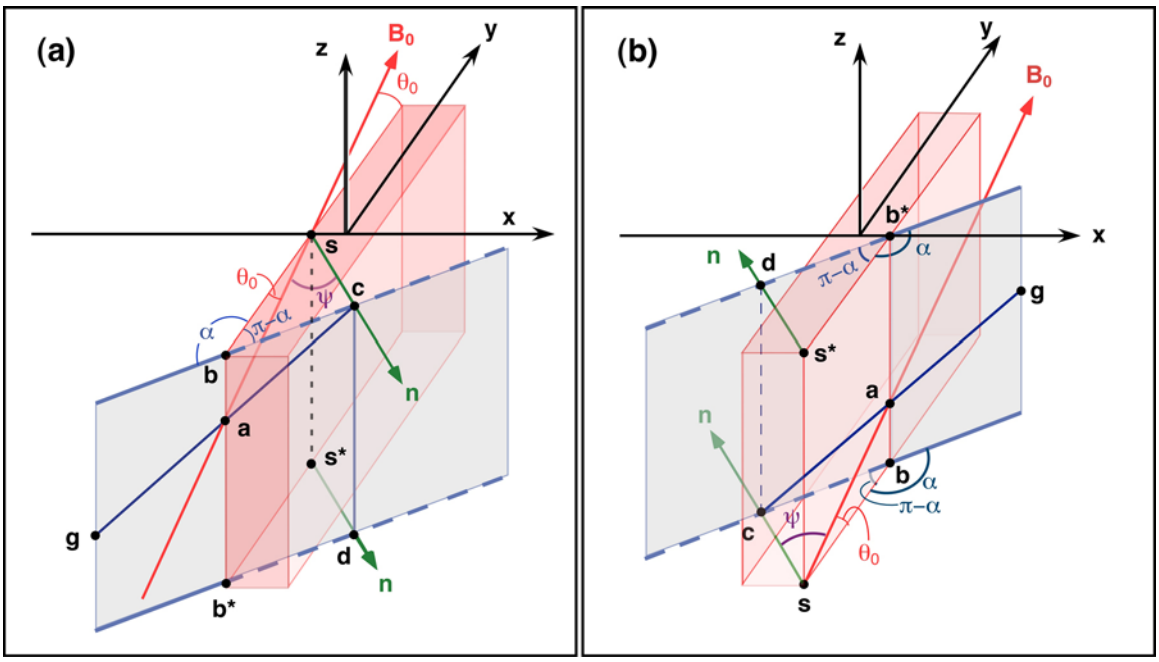

Figure 11. Sketches to show how to determine the flaring angle α of the slow-mode Mach-cone-like plane wave, which is generated by a line-type disturbance. The line-type disturbance moves toward (a) the $-y$ direction with respect to the uniform plasma in region 1 ($x < -(w_j + w)/2$) and (b) the $+y$ direction with respect to the uniform plasma in region 2 ($x > (w_j + w)/2$). See the text for the discussion in detail.

of the slow-mode plane wave that propagates along the plane wave normal direction (**n**), $C_{SL0\psi_g}$ is the speed of the corresponding group velocity of the slow-mode wave with phase velocity **n** $C_{SL0\psi}$, and C_{SL0y} defined by equation (11) is the phase speed of the slow-mode wave that propagates along the surface wave direction (**y**). Namely,

$$C^2_{SL0\psi} = \frac{1}{2}\left\{C^2_{A0} + C^2_{S0} - \sqrt{\left(C^2_{A0} + C^2_{S0}\right)^2 - 4C^2_{A0}C^2_{S0}\cos^2\psi}\right\} \tag{20}$$

$$C_{SL0\psi_g} = \sqrt{C^2_{SL0\psi} + \left(\frac{1}{2C_{SL0\psi}}\frac{dC^2_{SL0\psi}}{d\psi}\right)^2} \tag{21}$$

Note that, for the MHD waves, the phase speed $\omega/k = F(\theta)$ is not a function of wave number k. Thus, the group velocity, $\mathbf{V}_g = d\omega/d\mathbf{k}$, and the phase velocity, $\mathbf{V}_p = \mathbf{e}_k(\omega/k)$, satisfy the following relationship:

$$(\mathbf{V}_g - \mathbf{V}_p)\cdot\mathbf{V}_p = \left[\left(\mathbf{e}_k\frac{\partial\omega}{\partial k} + \mathbf{e}_\theta\frac{1}{k}\frac{\partial\omega}{\partial\theta}\right) - \mathbf{e}_k\frac{\omega}{k}\right]\cdot\mathbf{e}_k\frac{\omega}{k} = 0.$$

Therefore, we can conclude that the vector gc is always perpendicular to the wave normal vector sc. The surface of the tetrahedron $sabc$ consists of four right triangles, where three of them yield $sc/sa = \cos\psi$, $sc/sb = \sin(\pi - \alpha)$, and $sb/sa = \cos\theta_0$. Since $sc/sa = (sc/sb)\cdot(sb/sa)$, it yields

$$\cos\psi = \cos\theta_0\sin(\pi - \alpha) \tag{22}$$

where

$$\sin(\pi - \alpha) = \frac{sc}{sb} = \frac{C_{SL0\psi}}{M_{SL0y}C_{SL0y}} \tag{23}$$

and $C_{SL0\psi}$ and C_{SL0y} are given in equations (20) and (11), respectively.

[38] Substituting equation (22) into equation (20) then substituting the resulting equation and the equation (11) into the equation (23), it yields

$$C^2_{S0} + C^2_{A0} - 2M^2_{SL0y}C^2_{SL0y}\sin^2(\pi - \alpha) = \sqrt{\left(C^2_{A0} + C^2_{S0}\right)^2 - 4C^2_{A0}C^2_{S0}\cos^2\theta_0\sin^2(\pi - \alpha)} \tag{24}$$

Since the right-hand side of the equation (24) must be equal to or greater than zero, the left-hand side of equation (24) yields the following condition:

$$C^2_{S0} + C^2_{A0} - 2M^2_{SL0y}C^2_{SL0y}\sin^2(\pi - \alpha) \geq 0 \tag{25}$$

Solving equation (24) for $\sin^2(\pi - \alpha)$, it yields

$$\sin^2(\pi - \alpha) = \frac{C^2_{S0} + C^2_{A0}}{M^2_{SL0y}C^2_{SL0y}} - \frac{C^2_{S0}C^2_{A0}\cos^2\theta_0}{M^4_{SL0y}C^4_{SL0y}} \tag{26}$$

[39] For $0 \leq (C^2_{S0} + C^2_{A0})M^2_{SL0y}C^2_{SL0y} - C^2_{S0}C^2_{A0}\cos^2\theta_0 \leq M^4_{SL0y}C^4_{SL0y}$, equation (26) yields

$$\alpha = \pi - \sin^{-1}\sqrt{\frac{C^2_{S0} + C^2_{A0}}{M^2_{SL0y}C^2_{SL0y}} - \frac{C^2_{S0}C^2_{A0}\cos^2\theta_0}{M^4_{SL0y}C^4_{SL0y}}} \tag{27}$$

Only the solutions, which satisfy both the condition (25) and equation (27), will be considered as proper solutions.

[40] For $C_{S0}^2/C_{A0}^2 = \gamma\beta_0/2$, equation (27) can be rewritten as

$$\alpha = \pi - \sin^{-1}\sqrt{\frac{(\gamma\beta_0/2)+1}{M_{SL0y}^2\left(C_{SL0y}^2/C_{A0}^2\right)} - \frac{(\gamma\beta_0/2)\cos^2\theta_0}{M_{SL0y}^4\left(C_{SL0y}^2/C_{A0}^2\right)^2}} \tag{28}$$

where

$$\frac{C_{SL0y}^2}{C_{A0}^2} = \frac{1}{2}\left\{1 + \frac{\gamma\beta_0}{2} - \sqrt{\left(1+\frac{\gamma\beta_0}{2}\right)^2 - 2\gamma\beta_0\cos^2\theta_0}\right\} \tag{29}$$

Likewise, condition (25) can be rewritten as

$$\frac{\gamma\beta_0}{2} + 1 - 2M_{SL0y}^2\frac{C_{SL0y}^2}{C_{A0}^2}\sin^2(\pi-\alpha) \geq 0 \tag{30}$$

As we can see that the flaring angle α given in equation (28) is a function of M_{SL0y}, θ_0, and β_0. We also found that for a given set of M_{SL0y} and θ_0 the solutions of equation (28) obtained at $C_{S0}^2/C_{A0}^2 = \xi$ and at $C_{S0}^2/C_{A0}^2 = 1/\xi$ are always identical to each other.

[41] Figure 12 shows the theoretical solutions of the flaring angles α as a function of M_{SL0y}, β_0, and θ_0, where Figure 12a is for $\theta_0 = 0°$ and Figure 12b is for $\theta_0 = 20°$. The three curves in Figures 12a and 12b are the theoretical solutions obtained at $\beta_0 = 2.4$ (dashed curve), $\beta_0 = 0.89$ (thin curve), and $\beta_0 = 1.17$ (thick curve). Solutions shown in Figure 12 satisfy equation (28) and condition (30). The symbols shown in Figure 12 are the flaring angles of the nonlinear plane waves measured from our simulation results with the corresponding β_0, M_{SL0y}, and θ_0. The open square is for $\beta_0 = 2.4$. The solid circle is for $\beta_0 = 0.89$. The open circle is for $\beta_0 = 1.17$. The flaring angles measured from our simulation results are in good agreements with the predicted flaring angles obtained from equation (28) and condition (30).

[42] The theoretical results shown in Figure 12 indicate that the theoretical solutions cannot be found when the slow-mode Mach numbers of the surface waves are greater than one or much less than one. The solution space in M_{SL0y} actually depends on θ_0 and β_0. As we can see, for $\theta_0 = 0°$ and $\beta_0 \approx 1.2$, the slow-mode plane wave can be found in a wide range of M_{SL0y}, much wider than the solution space at $\theta_0 = 20°$ and $\beta_0 \gg 1.2$ or $\beta_0 \ll 1.2$. Indeed, we found that the slow-mode nonlinear plane waves can be easily formed in our simulations with $\beta_0 \approx 1.2$ and $\theta_0 \approx 0°$ or $\theta_0 \approx 180°$, even with slightly perturbations on the surface wave speed.

5. Summary

[43] In our two-dimensional MHD simulation of the jet-flow-associated K-H instability, four types of nonlinear waves are found at the saturation stage. The first type of the nonlinear waves is characterized by vortex structures with opposite vorticities generated in pairs. It occurs when the fast-mode Mach numbers of the surface waves (M_{F0y}) on both sides of the jet flow are less than one and the intermediate-mode Mach numbers of the surface waves (M_{I0y}) on both sides of the jet flow are greater than one, and when the magnetic fields on both sides of the TD are nearly perpendicular to the surface wave propagation direction.

[44] The second type is the S-shaped surface wave. It occurs when the fast-mode Mach numbers of the surface waves (M_{F0y}) on both sides of the jet flow are less than one and the intermediate-mode Mach numbers of the surface waves (M_{I0y}) on both sides of the jet flow are greater than one, and when the magnetic fields on both sides of the TD are nearly parallel to the surface wave propagation direction.

[45] The third type of the nonlinear waves is characterized by fast-mode nonlinear plane waves, which are launched from the ridges of the S-shaped surface waves in pairs. It occurs when the fast-mode Mach numbers of the surface waves (M_{F0y}) on both sides of the jet flow are equal to or greater than one. The distributions of the fast-mode plane waves are similar to the nonlinear structures obtained in the laboratory experiment of jet flow by *Papamoschou and Roshko* [1988]. Our results are also similar to the shock-like structures obtained in previous MHD simulation studies of jet flow in the stellar medium [e.g., *Baty and Keppens*, 2002, 2006].

[46] The fourth type of the nonlinear waves is characterized by the slow-mode nonlinear plane waves, which are launched from the ridges of the S-shaped surface waves in pairs. To our knowledge, this is the first report of slow-mode nonlinear solitary waves found in the simulations of the K-H instability. The slow-mode plane waves can be found in a limited range of M_{SL0y}, β_0, and θ_0. No slow-mode plane wave can be found when the slow-mode Mach number of the surface wave (M_{SL0y}) is greater than one.

[47] A theoretical model, which is a simplified linear wave interference model, has been proposed in section 4 to explain the formation of the nonlinear plane waves found in this simulation study. Namely, fast-mode waves and slow-mode waves will be emitted from the ridges of the surface perturbations and expand based on their group velocities. According to our model, the fast-mode plane waves and the slow-mode plane waves are generated by the constructive interferences of the fast-mode waves and the slow-mode waves, respectively, under the proper conditions of M_{F0y}, M_{SL0y}, β_0, and θ_0. Since the distribution of the slow-mode group velocity is quite different from the distribution of the fast-mode group velocity, the geometry of the fast-mode nonlinear plane waves and slow-mode nonlinear plane waves also looks very different from each other. The Λ-shaped fast-mode Mach-cone-like plane waves can be found when $M_{F0y} \geq 1$. The V-shaped slow-mode Mach-cone-like plane waves can be found in a limited range of M_{SL0y}, β_0, and θ_0. The flaring angle is less than or equal to 90° for the fast-mode Mach-cone-like nonlinear waves. The flaring angle is greater than or equal to 90° for the slow-mode Mach-cone-like nonlinear waves.

[48] The flaring angle of the slow-mode plane wave is derived analytically as a function of M_{SL0y}, β_0, and θ_0. The flaring angles of the slow-mode plane waves measured from our simulation results are in good agreements with the theoretical solutions. No solution can be found when the

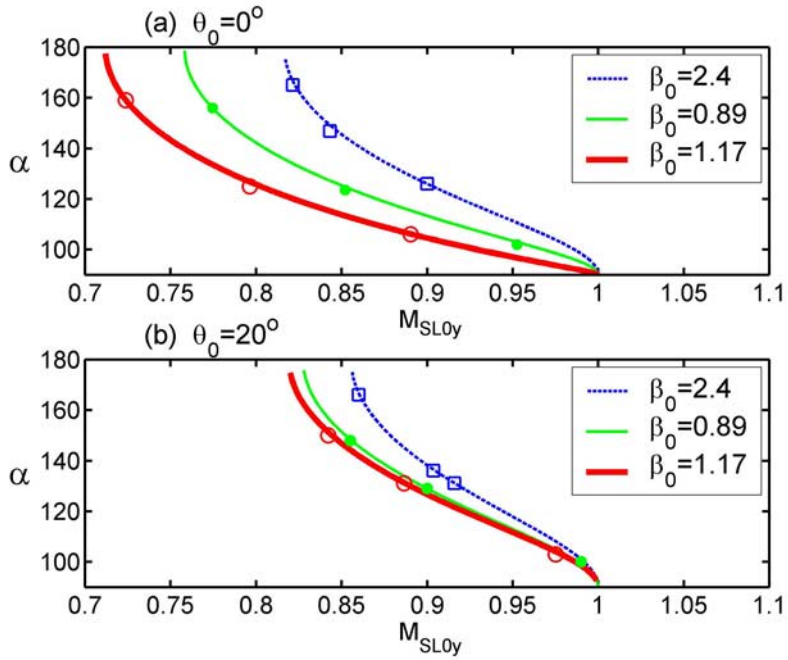

Figure 12. Plots of the flaring angles predicted by the theoretical model and measured from the simulation results. The theoretical solution of the flaring angle α obtained from equations (28)–(30) is a function of M_{SL0y}, β_0, and θ_0. We plot the flaring angle α as a function of M_{SL0y}, at given β_0, and θ_0, where (a) $\theta_0 = 0^\circ$ and (b) $\theta_0 = 20^\circ$. The three curves in Figures 12a and 12b are the theoretical solutions obtained at $\beta_0 = 2.4$ (dashed curve), $\beta_0 = 0.89$ (thin curve), and $\beta_0 = 1.17$ (thick curve). The symbols shown in this figure are the flaring angles of the slow-mode nonlinear plane waves measured from our simulation results with the corresponding β_0, M_{SL0y}, and θ_0, where the open squares are for $\beta_0 = 2.4$, the solid circles are for $\beta_0 = 0.89$, and the open circles are for $\beta_0 = 1.17$. The flaring angles measured from our simulation results are in good agreement with the predicted flaring angles obtained from equation (28) and condition (30).

slow-mode Mach numbers of the surface waves are greater than one ($M_{SL0y} > 1$). According to the solution space at different β_0, the slow-mode plane waves should be easily found in the cases with $\beta_0 \sim 1.2$ and $\theta_0 \approx 0^\circ$ or $\theta_0 \approx 180^\circ$. The solution space of the flaring angle α obtained from equation (28) and condition (30) can provide a good explanation to the reason why the slow-mode plane waves in our simulation can only be found in a limited range of M_{SL0y}, β_0, and θ_0.

6. Discussions

[49] The possible applications of our results to the space observations are discussed below. According to our simulation results, we propose that the slow-mode Mach-cone-like nonlinear waves and the fast-mode Mach-cone-like nonlinear waves are likely found near the fast-flow regions observed at the dayside magnetopause or in the magnetotail. The nonlinear Mach-cone-like plane waves should also be found near the boundaries of the fast solar wind and the slow solar wind, which is also called the corotating interaction regions (CIRs). But we also expect that a nonuniform magnetic field or nonuniform plasma density in region 1 or region 2 can lead to wave mode conversion in these regions. The wave mode conversion in a nonuniform medium can excite new wave modes and redirect the wave energy to different directions. The reflection of the nonlinear Mach-cone-like plane waves from the nearby boundary can lead to another kind of turbulent structure.

[50] Figure 13 shows two examples of the refraction of the fast-mode Mach-cone-like plane waves when the waves expand into a non-uniform background medium. Figure 13a shows that the fast-mode Mach-cone-like plane waves expand into a dense medium at $x > 20w$. As we can see, the refraction angle of the nonlinear plane waves is smaller than the incident angle. The plane waves are partially reflected by the dense medium. Figure 13b shows that the fast-mode Mach-cone-like plane waves expand into a rarefied medium at $x > 10w$. As we can see, the refraction angle of the nonlinear plane waves is nearly 90°. Note that the coexistence of incident and reflected waves has also been shown in previous simulations of KH instability for super magnetosonic shear flows [e.g., *Miura*, 1990, 1992]. Although the reflection of the incident wave in the previous studies is due to the existence of a numerical boundary, the interference of the incident and reflected waves are similar to the one shown in Figure 13a.

[51] Since the eigenvectors of the three MHD wave modes change their directions with changing directions of the background magnetic field, wave mode conversions are expected to take place if there was a gradual change on the magnetic field direction in region 1 or region 2. The wave mode conversion is an interesting research topic, but it is beyond the scope of this study. Nevertheless, we could

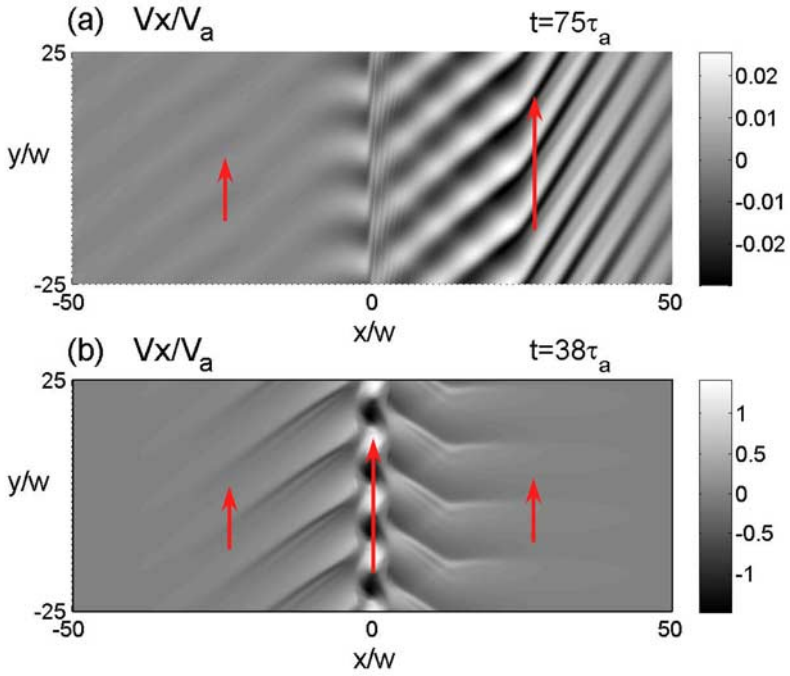

Figure 13. Two examples to show the refraction of the fast-mode Mach-cone-like plane waves when the waves expand into a non-uniform background medium. The arrows indicate the background flow distributions observed in the simulation rest frame. (a) The fast-mode Mach-cone-like plane waves expand into a dense medium at $x > 20w$. As we can see, the refraction angle of the nonlinear plane waves is smaller than the incident angle. The plane waves are partially reflected by the dense medium. (b) The fast-mode Mach-cone-like plane waves expand into a rarefied medium at $x > 10w$. As we can see, the refraction angle of the nonlinear plane waves is nearly 90°.

expect that the nonlinear Mach-cone-like plane waves, generated by the velocity shear instability in the solar wind or at the magnetopause, should directly or indirectly contribute to the turbulent structures observed in the solar wind and in the magnetosheath.

[52] The limitations of our simulation and theoretical results are discussed below. The Mach numbers of the surface disturbances can be greater than 1 or less than 1, but the Mach numbers of the Mach-cone-like plane waves are always equal to one. Therefore, these Mach-cone-like plane waves are weak nonlinear solitary waves. This may be the reason why the theoretical model based on the constructive interference of linear waves can successfully explain the flaring angles of these weak nonlinear solitary waves. Since the superposition assumption is not applicable to a highly nonlinear event, the simple theoretical model proposed in this paper might not be able to explain the distribution and evolution of the shock waves, if we could find one in the future study.

[53] Owing to lack of effective dissipation in our simulation, we cannot reproduce the shock wave structures as have been reported in previous simulation studies [e.g., *Miura*, 1982, 1984]. We do not want to use the MHD model to simulate the formation of shock waves because we believe that only the kinetic simulations can properly simulate the anomalous dissipation process associated with the shock formations in the collisionless space plasma.

[54] Dispersion effect due to finite-ion-inertial-length effect is not included in this study. The dispersion effect can lead to formation of whistler waves and kinetic Alfvén waves. It can also lead to formation of six types of solitary waves as have been obtained by *Lyu and Kan* [1989]. The magnetic field profile of the solitary waves obtained in the present study are linearly polarized, which are different from the magnetic field polarizations found in the two-fluid solitary waves analysis by *Lyu and Kan* [1989]. The magnetic field profile across the two-fluid solitary wave is either left-hand polarized or right-hand polarized. In order to obtain the solitary waves as discussed by *Lyu and Kan* [1989], the finite-ion-inertial-length effect should be included in the simulation.

[55] **Acknowledgments.** This work is supported by the NSC grants 95-2111-M-008-021 and 96-2111-M-008-014 to the National Central University, the NSPO grants 95-NSPO(B)-SP-FA07-01(C) and 96-NSPO(B)-SP-FA07-01(D) to the National Central University, and the MOE grant "Aim for the Top University" to the National Central University.

[56] Amitava Bhattacharjee thanks the reviewers for their assistance in evaluating this paper.

References

Angelopoulos, V., W. Baumjohann, C. F. Kennel, F. V. Coroniti, M. G. Kivelson, R. Pellat, R. J. Walker, H. Lühr, and G. Paschmann (1992), Bursty bulk flows in the inner central plasma sheet, *J. Geophys. Res.*, *97*, 4027, doi:10.1029/91JA02701.

Angelopoulos, V., C. F. Kennel, F. V. Coroniti, R. Pellat, M. G. Kivelson, R. J. Walker, C. T. Russell, W. Baumjohann, W. C. Feldman, and J. T. Gosling (1994), Statistical characteristics of bursty bulk flow events, *J. Geophys. Res.*, *99*, 21,257, doi:10.1029/94JA01263.

Angelopoulos, V., et al. (1996), Multipoint analysis of a bursty bulk flow event on April 11, 1985, *J. Geophys. Res.*, *101*, 4967, doi:10.1029/95JA02722.

Angelopoulos, V., F. S. Mozer, T. Mukai, K. Tsuruda, S. Kokubun, and T. J. Hughes (1999), On the relationship between bursty flows, current disruption and substorms, *Geophys. Res. Lett.*, *26*, 2841, doi:10.1029/1999GL900601.

Baty, H., and R. Keppens (2002), Interplay between Kelvin-Helmholtz and current-driven instabilities in jets, *Astrophys. J.*, *580*, 800, doi:10.1086/343893.

Baty, H., and R. Keppens (2006), Kelvin-Helmholtz disruptions in extended magnetized jet flows, *Astron. Astrophys.*, *447*, 9, doi:10.1051/0004-6361:20053969.

Baumjohann, W., G. Paschmann, and H. Lühr (1990), Characteristics of high-speed ion flows in the plasma sheet, *J. Geophys. Res.*, *95*, 3801, doi:10.1029/JA095iA04p03801.

Bodo, G., S. Massaglia, A. Ferrari, and E. Trussoni (1994), Kelvin-Helmholtz instability of hydrodynamic supersonic jets, *Astron. Astrophys.*, *283*, 655.

Bodo, G., S. Massaglia, P. Rossi, R. Rosner, A. Malagoli, and A. Ferrari (1995), The long-term evolution and mixing properties of high Mach number hydrodynamic jets, *Astron. Astrophys.*, *303*, 281.

Cao, J. B., et al. (2006), Joint observations by Cluster satellites of bursty bulk flows in the magnetotail, *J. Geophys. Res.*, *111*, A04206, doi:10.1029/2005JA011322.

Chen, S.-H., and M. G. Kivelson (1993), On nonsinusoidal waves at the Earth's magnetopause, *Geophys. Res. Lett.*, *20*, 2699, doi:10.1029/93GL02622.

Chen, S.-H., M. G. Kivelson, J. T. Gosling, R. J. Walker, and A. J. Lazarus (1993), Anomalous aspects of magnetosheath flow and of the shape and oscillations of the magnetopause during an interval of strongly northward interplanetary magnetic field, *J. Geophys. Res.*, *98*, 5727, doi:10.1029/92JA02263.

Huang, C. Y., and L. A. Frank (1986), A statistical study of the central plasma sheet: Implications for substorm models, *Geophys. Res. Lett.*, *13*, 652, doi:10.1029/GL013i007p00652.

Lai, S. H., and L. H. Lyu (2006), Nonlinear evolution of the MHD Kelvin-Helmholtz instability in a compressible plasma, *J. Geophys. Res.*, *111*, A01202, doi:10.1029/2004JA010724.

Landau, L. D., and E. M. Lifshitz (1987), *Fluid Mechanics*, 2nd ed., Pergamon, Oxford, U. K.

Lui, A. T. Y., E. W. Hones Jr., F. Yasuhara, S.-I. Akasofu, and S. J. Bame (1977), Magnetotail plasma flow during plasma sheet expansions: VELA 5 and 6 and IMP 6 observations, *J. Geophys. Res.*, *82*, 1235, doi:10.1029/JA082i007p01235.

Lyu, L. H., and J. R. Kan (1989), Nonlinear two-fluid hydromagnetic waves in the solar wind: Rotational discontinuity, soliton, and finite-extent Alfven wave train solutions, *J. Geophys. Res.*, *94*, 6523, doi:10.1029/JA094iA06p06523.

Manuel, J. R., and J. C. Samson (1993), The spatial development of the low-latitude boundary layer, *J. Geophys. Res.*, *98*, 17,367, doi:10.1029/93JA01524.

Martí, J.-M., M. Perucho, and M. Hanasz (2004), Stability of relativistic hydrodynamical planar jets: Linear and nonlinear evolution of Kelvin-Helmholtz modes, *Astrophys. Space Sci.*, *293*, 139, doi:10.1023/B:ASTR.0000044661.74221.59.

Miura, A. (1982), Nonlinear evolution of the magnetohydrodynamic Kelvin-Helmholtz instability, *Phys. Rev. Lett.*, *49*, 779, doi:10.1103/PhysRevLett.49.779.

Miura, A. (1984), Anomalous transport by magnetohydrodynamic Kelvin-Helmholtz instabilities in the solar wind-Magnetosphere interaction, *J. Geophys. Res.*, *89*, 801, doi:10.1029/JA089iA02p00801.

Miura, A. (1987), Simulation of Kelvin-Helmholtz instability at the magnetospheric boundary, *J. Geophys. Res.*, *92*, 3195, doi:10.1029/JA092iA04p03195.

Miura, A. (1990), Kelvin-Helmholtz instability for supersonic shear flow at the magnetospheric boundary, *Geophys. Res. Lett.*, *17*, 749, doi:10.1029/GL017i006p00749.

Miura, A. (1992), Kelvin-Helmholtz instability at the magnetospheric boundary: Dependence on the magnetosheath sonic Mach number, *J. Geophys. Res.*, *97*, 10,655, doi:10.1029/92JA00791.

Miura, A. (1995), Kelvin-Helmholtz instability at the magnetopause: Computer simulations, in *Physics of the Magnetopause*, *Geophys. Monogr. Ser.*, vol. 90, edited by P. Song, B. U. Ö. Sonnerup, and M. F. Thomsen, pp. 285–291, AGU, Washington, D. C.

Miura, A. (1997), Compressible magnetohydrodynamic Kelvin-Helmholtz instability with vortex pairing in the two-dimensional transverse configuration, *Phys. Plasmas*, *4*, 2871, doi:10.1063/1.872419.

Miura, A. (1999), Self-organization in the two-dimensional magnetohydrodynamic transverse Kelvin-Helmholtz instability, *J. Geophys. Res.*, *104*, 395, doi:10.1029/98JA02530.

Nakamura, M., G. Paschmann, W. Baumjohann, and N. Sckopke (1991), Ion distributions and flows near the neutral sheet, *J. Geophys. Res.*, *96*, 5631, doi:10.1029/90JA02495.

Nakamura, R., W. Baumjohann, R. Schödel, M. Brittnacher, V. A. Sergeev, M. Kubyshkina, T. Mukai, and K. Liou (2001), Earthward flow bursts, auroral streamers, and small expansions, *J. Geophys. Res.*, *106*, 10,791, doi:10.1029/2000JA000306.

Norman, M. L., L. Smarr, K.-H. A. Winkler, and M. D. Smith (1982), Structure and dynamics of supersonic jets, *Astron. Astrophys.*, *113*, 285.

Otto, A., and D. H. Fairfield (2000), Kelvin-Helmholtz instability at the magnetotail boundary: MHD simulation and comparison with Geotail observations, *J. Geophys. Res.*, *105*, 21,175, doi:10.1029/1999JA000312.

Papamoschou, D., and A. Roshko (1988), The compressible turbulent shear layer: An experimental study, *J. Fluid Mech.*, *197*, 453, doi:10.1017/S0022112088003325.

Paschmann, G., B. U. Ö. Sonnerup, I. Papamastorakis, N. Sckopke, G. Haerendel, S. J. Bame, J. R. Asbridge, J. T. Gosling, C. T. Russell, and R. C. Elphic (1979), Plasma acceleration at the Earth's magnetopause: Evidence for reconnection, *Nature*, *282*, 243, doi:10.1038/282243a0.

Slavin, J. A., et al. (1997), WIND, GEOTAIL, and GOES 9 observations of magnetic field dipolarization and bursty bulk flows in the near-tail, *Geophys. Res. Lett.*, *24*, 971, doi:10.1029/97GL00542.

Thomas, V. A. (1995), Kinetic simulation of the Kelvin-Helmholtz instability in a finite sized jet, *J. Geophys. Res.*, *100*, 12,011, doi:10.1029/94JA02371.

Thomas, V. A., and D. Winske (1993), Kinetic simulations of the Kelvin-Helmholtz instability at the magnetopause, *J. Geophys. Res.*, *98*, 11,425, doi:10.1029/93JA00604.

Wu, C. C. (1986), Kelvin-Helmholtz instability at the magnetopause boundary, *J. Geophys. Res.*, *91*, 3042, doi:10.1029/JA091iA03p03042.

Yoon, P. H., J. F. Drake, and A. T. Y. Lui (1996), Theory and simulaiton of Kelvin-Helmholtz instability in the geomagnetic tail, *J. Geophys. Res.*, *101*, 27,327, doi:10.1029/96JA02752.

S. H. Lai and L. H. Lyu, Institute of Space Science, National Central University, Chung-Li, 32054, Taiwan. (lyu@jupiter.ss.ncu.edu.tw)